JOURNAL OF GEOPHYSICAL RESEARCH, VOL. 114, B06208, doi:10.1029/2008JB005890, 2009

Seismic wave attenuation in carbonates

L. Adam,[1,2] M. Batzle,[3] K. T. Lewallen,[4] and K. van Wijk[1]

Received 23 June 2008; revised 7 December 2008; accepted 22 January 2009; published 25 June 2009.

[1] The effect of pore fluids on seismic wave attenuation in carbonate rocks is important for interpreting remote sensing observations of carbonate reservoirs undergoing enhanced oil recovery. Here we measure the elastic moduli and attenuation in the laboratory for five carbonate samples with 20% to 30% porosity and permeability between 0.03 and 58.1 mdarcy. Contrary to most observations in sandstones, bulk compressibility losses dominate over shear wave losses for dry samples and samples fully saturated with either liquid butane or brine. This observation holds for four out of five samples at seismic (10–1000 Hz) and ultrasonic frequencies (0.8 MHz) and reservoir pressures. Attenuation modeled from the modulus data using Cole-Cole relations agrees in that the bulk losses are greater than the shear losses. On average, attenuation increases by 250% when brine substitutes a light hydrocarbon in these carbonate rocks. For some of our samples, attenuation is frequency-dependent, but in the typical exploration frequency range (10–100 Hz), attenuation is practically constant for the measured samples.

Citation: Adam, L., M. Batzle, K. T. Lewallen, and K. van Wijk (2009), Seismic wave attenuation in carbonates, *J. Geophys. Res.*, *114*, B06208, doi:10.1029/2008JB005890.

1. Introduction

[2] Velocity and amplitude analysis of elastic waves is common practice in reservoir rock physics. Variations in reservoir seismic properties can be related to fluid changes within them. Intrinsic wave attenuation, or the conversion of mechanical energy into heat, has been a topic of research for many years. Although numerous studies examine mostly clastic rocks [*Winkler and Nur*, 1982; *Best et al.*, 1994; *Murphy*, 1982; *Wyllie et al.*, 1962; *Spencer*, 1979; *Best et al.*, 2007], there are few laboratory measurements of attenuation in carbonates rocks, and even fewer experimental data at exploration seismic frequencies and reservoir pressures [*Lienert and Manghnani*, 1990; *Paffenholz and Burkhardt*, 1989; *Spencer*, 1981; *Batzle et al.*, 2005; *Gautam*, 2003]. Because more than half of the current major oil and gas reservoirs in the world are in carbonates, these rocks have become important topics of rock property research. Our study analyzes wave attenuation in five carbonate samples at seismic frequencies (10^1–10^3 Hz), and at an ultrasonic frequency (10^6 Hz) for three of the samples. The rocks are measured dry and fully saturated with a light hydrocarbon and with a brine, at reservoir pressures.

[3] There are several ways to describe intrinsic seismic losses, and in this paper we use the definition of attenuation as the inverse of the quality factor (Q). Intrinsic attenuation can be defined as $Q^{-1} = \mathrm{Im}[M^*]/\mathrm{Re}[M^*]$, where M^* is the complex modulus or velocity; and the imaginary part (Im) of the complex modulus is small. Different waves and flexural modes allow us to study the shear wave (Q_S^{-1}), compressional wave (Q_P^{-1}), extensional (Q_E^{-1}) and bulk compressibility (Q_K^{-1}) attenuation. *Winkler and Nur* [1979] and *Winkler* [1979] analytically show that one of the following relations between the attenuation modes will always be true:

$$Q_S^{-1} > Q_E^{-1} > Q_P^{-1} > Q_K^{-1}, \tag{1}$$

$$Q_K^{-1} > Q_P^{-1} > Q_E^{-1} > Q_S^{-1}, \tag{2}$$

$$Q_K^{-1} = Q_P^{-1} = Q_E^{-1} = Q_S^{-1}. \tag{3}$$

[4] For a porous medium and on the basis of the conceptual model of two identical cracks perpendicular to each other and touching at their tips, *Winkler* [1979] interprets relation (1) as the expected behavior when the rock is fully saturated, while equation (2) is for partially saturated rocks. This is generally true in sandstones for either sonic or ultrasonic frequencies: the shear losses at full saturation are mostly observed to be greater than the bulk or compressional wave losses [*Winkler and Nur*, 1982; *Best et al.*, 1994; *Murphy*, 1982; *Wyllie et al.*, 1962; *Spencer*, 1979; *Toksoz et al.*, 1979]. Pore shape and distribution in sandstone could dictate that either P wave or S wave attenuation can dominate at logging frequencies [*Assefa et al.*, 1999; *Prasad and Meissner*, 1992].

[1]Department of Geosciences, Boise State University, Boise, Idaho, USA.
[2]Formerly at Department of Geophysics, Colorado School of Mines, Golden, Colorado, USA.
[3]Department of Geophysics, Colorado School of Mines, Golden, Colorado, USA.
[4]ExxonMobil Upstream Research Company, Houston, Texas, USA.

0148-0227/09/2008JB005890$09.00

Table 1. Petrological Data for the Carbonate Set[a]

	Samples				
	100	200	300	B	C
Porosity (%)	32.79	30.46	20.39	4.60	21.00
Permeability (mdarcy)	6.75	5.19	58.10	0.03	5.50
Grain density (g/cm^3)	2.71	2.71	2.71	2.84	2.70
Calcite (%)	90.6	89.4	98.6	0.7	75.8
Dolomite (%)	8.5	9.6	TR	97.0	20.6
Quartz (%)	0.6	0.7	1.2	0.6	1.2
Phyllosilicates (%)	0.0	TR	TR	0.8	2.4
Texture	wacke	wacke	pack	mud	grain
Depth (m)	2479	2452	2456	3181	3138
Reservoir Pd (MPa)	34.5	34.5	34.5	35.8	35.8
Heterogeneity	none	none	vertical bands	horizontal bands	none

[a]Mineralogy was obtained from XRD analysis and are reported in percent per volume. TR means less than 0.3%. Texture follows modified Dunham's carbonate classification [*Moore*, 2001]: mud, mudstone; wacke, wackestone; pack, packstone; and grain, grainstone. Porosity and permeability are measured at 18.3 MPa confining pressure for samples 100, 200, and 300 and at reservoir pressures for samples B and C. By heterogeneity we refer to visual or CT scan heterogeneous features.

[5] However, published data on carbonates are mixed regarding which attenuation mode dominates. *Lucet* [1989] and *Lucet et al.* [1991] measured Q_E^{-1} and Q_S^{-1} on 15 saturated limestones at sonic and ultrasonic frequencies. $Q_E^{-1} > Q_S^{-1}$ for virtually all the fully water saturated samples. *Paffenholz and Burkhardt* [1989] and *Cadoret et al.* [1998] observe that $Q_E^{-1} > Q_S^{-1}$ at seismic and sonic frequencies respectively for water-saturated samples. Recently, *Best et al.* [2007] and *Agersborg et al.* [2008] measured carbonate samples at ultrasonic frequencies and high differential pressures. Differential pressure is the difference between hydrostatic confining pressure and pore pressure. The three carbonate samples from *Best et al.* [2007] show mixed relations between Q_P^{-1} and Q_S^{-1}, because the samples have velocity and attenuation anisotropy resulting from the complex pore structure. Four out of the six samples from *Agersborg et al.* [2008] have estimates of Q_P^{-1} greater than Q_S^{-1} under dry and fully brine saturated conditions at 30 MPa differential pressure. Most of the previous work, except for *Lucet* [1989] and *Assefa et al.* [1999], has been performed at room conditions and with the samples either dry or saturated with water and measured at high frequencies. Here we study samples near the reservoir differential pressures over a broad frequency range, dry and saturated with brine, as well as with a light hydrocarbon for the purpose of reservoir characterization. For our fully saturated carbonate samples, the correlation among the different attenuation modes is described by relation (2).

[6] For our carbonate sample set, we address five important relationships. Specifically, we examine the relation between the modes of attenuation, compare Q at seismic and ultrasonic frequencies, measure the sensitivity of Q to fluids (either a light hydrocarbon or a brine), investigate the frequency dependence of Q in the exploration seismic bandwidth (10–100 Hz), and determine if there is a correlation between attenuation and permeability. Both the sensitivity of attenuation to fluids and its correlation to permeability are important for studying the evolution of reservoir systems, because one possible application for utilizing attenuation as a monitoring tool is during enhanced oil recovery where water, steam or CO_2 is injected into the reservoir to stimulate oil production. Although quantitative intrinsic attenuation data from surface seismic have been an interpretive challenge historically, characterizing attenuation becomes more robust as acquisition and processing technologies continue to improve.

2. Samples

[7] The core samples in this study come from two Middle Eastern carbonate reservoirs undergoing enhanced oil recovery. The core plugs from the first reservoir are samples 100, 200, and 300. For this field, light hydrocarbon production is stimulated by injecting brine into the reservoir [*Soroka et al.*, 2005]. Samples from the second reservoir are named B and C; corresponding to the same samples as in the work by *Adam et al.* [2006]. The samples are either almost pure calcite or dolomite (>95% total volume), with less than 3% clays. Table 1 summarizes the petrographical analysis. Porosity and permeability are measured using standard helium porosimetry and air permeability equipment. Permeability values are corrected for Klinkenberg gas slippage. The samples are cylindrical, and either 2.5 or 3.75 cm in diameter, with lengths varying from 4.3 to 5.5 cm. We now describe the petrographical characteristics of the samples, and thin sections for the samples are shown in Figure 1.

[8] Sample 100 has a mud-supported wackestone texture. Blue haze in the thin sections implies abundant microporosity (Figure 1). The presence of microporosity suggests the sample has a large content of irreducible water in situ. Micropores are 1–5 μm. The main fossil observed is Orbitolina. The sample is mostly calcite with calcite cement. Dolomite is deposited in small vugs after the dissolution of calcite (burial dolomite). It contains autogenic quartz and linear clam fragments [*Scholle and Ulmer-Scholle*, 2003].

[9] Sample 200 also has a mud-supported wackestone texture. This sample is similar to sample 100, except that micropores are larger (20–50 μm). The sample is partially burrowed and dolomite crystals are less coarse. This sample has larger amounts of fossils fragments than sample 100 (e.g., rudist fragments [*Scholle and Ulmer-Scholle*, 2003]).

[10] Sample 300 has a packstone borderline grainstone texture with abundant skeletal debris with inter-particle porosity. This type of porosity results in better permeability. Echinoderm fossils are surrounded by a synaxial overgrowth of calcite cement. Different textures between stylolytes are probably the result of high- and low-energy environments.

[11] Sample B has a mudstone texture, composed of relatively pure dolomite with a nonplanar fabric and a unimodal, aphanocrystalline to very finely crystalline structure. The sample has horizontal solution seams (or microstylolites) and small vugs (<1 mm), possibly infilled by an iron oxide.

[12] Sample C has a skeletal grainstone texture with finely crystalline spar matrix. Skeletal grains have been largely dissolved, but those remaining are foraminifera (mostly miliolids and other rotalids), ranging from 0.25 to 1.5 mm in diameter, moderately sorted. Contains moldic porosity, partially filled with euhedral dolomite rhombs (30–60 μm in diameter), and interparticle porosity, partially filled with subhedral finely crystalline calcite.

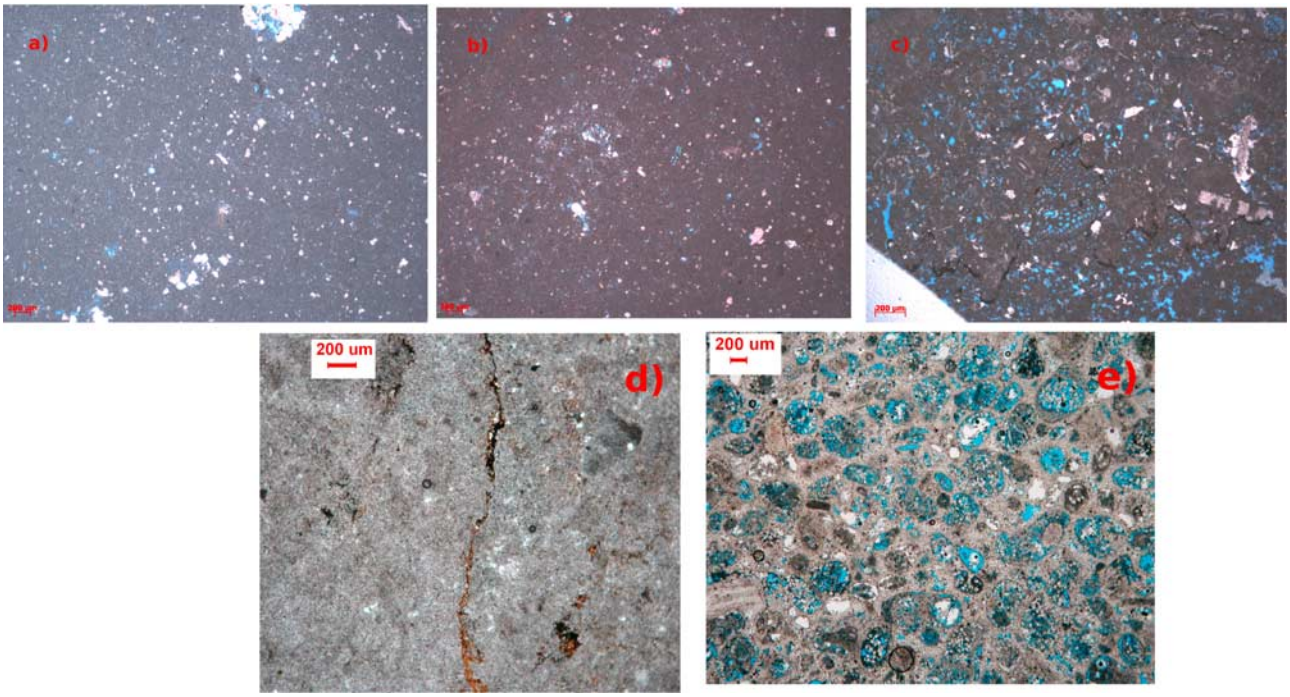

Figure 1. Thin section of samples (a) 100, (b) 200, (c) (300, (d) B, and (e) C. Shown in plane polarized light. Dyed epoxy is blue and represents pore space.

[13] On the basis of the fossil types, samples 100, 200, and 300 were deposited in the photolytic zone. In all three samples the cement is calcite and there are no clays.

[14] Samples 100 and 200 are similar in most petrographic aspects, with the main difference being the pore size estimated from the digital thin section images. Sample 100 has 1–5 μm pores, compared to 20–50 μm for sample 200. Small radius pores ($\sim$10 μm) generally have small pore throats, while larger radius pores (>10 μm) could either have large or small pore throats [*Lindquist et al.*, 2000]. Thus, sample 200 may have larger pore throats than sample 100. Pore throats are important, as they control the time fluid pressure takes to reach equilibrium after being disturbed by a passing wave. This fluid pressure disequilibrium controls attenuation. Figure 2 shows the CT scans of the samples. Gray scales represent densities contrasts. Sample 300 is the most heterogeneous, with vertical textural bands. Although we do not have the CT scan for sample 100, the scanning electron microscope (SEM), thin section and visual inspection show similarities to sample 200. Sample C, in spite of abundant fossils, is overall homogeneous. Finally, Figure 3 contains the SEM images of samples 100, 200, and 300. Crystals of dolomite are observed for samples 100 and 200 but are mostly absent for sample 300, verifying the XRD data (Table 1).

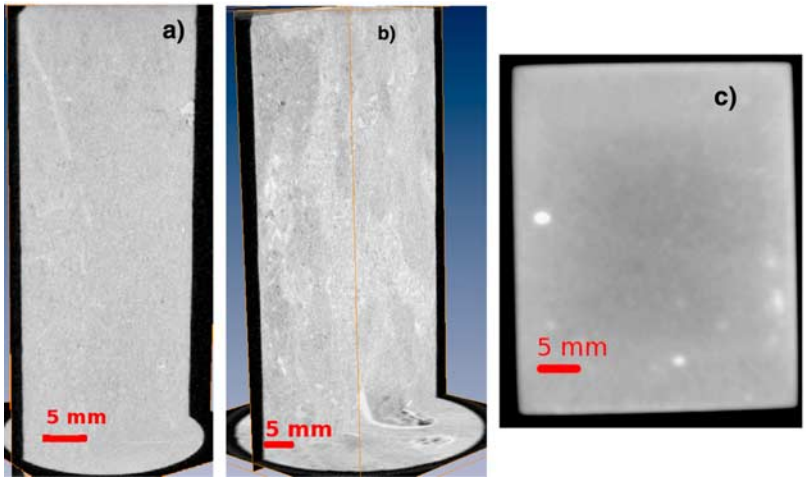

Figure 2. CT scans of samples (a) 200, (b) 300, and (c) B. Gray color variations represent density contrasts. Observe how sample 300 is heterogeneous with bands of different textures/porosity.

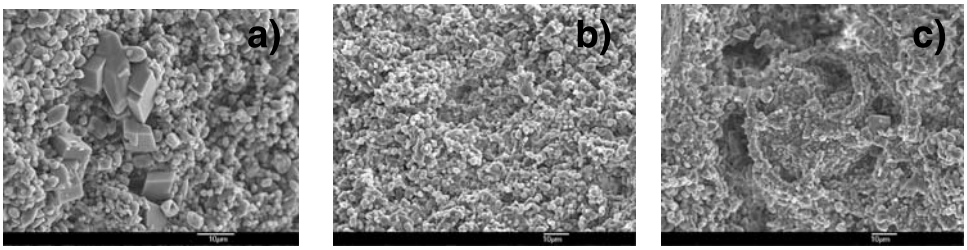

Figure 3. Scanning electron microscope (SEM) for samples (a) 100, (b) 200, and (c) 300. Sample 100 shows dolomite crystals. There are no SEM images for samples B and C.

[15] Velocity and attenuation anisotropy is not expected to be significant on these samples based on CT scans and visual inspection. Still, we do not quantitatively show the presence or absence of anisotropy.

3. Experimental Procedure

[16] The core samples are measured dry (humidified, as described below), 100% saturated with liquid butane (C_4H_{10}, a light hydrocarbon) or with high-salinity brine (180,000 ppm NaCl). Samples are first measured dry, then butane is injected into the sample until there is no more flow from the fluid pump to the sample, indicating we have reached a full saturation state. Butane at room conditions is a gas, but becomes liquid at pressures greater than 0.3 MPa. To remove the liquid butane from the sample pore space, we slowly decrease the pore pressure until we reach the room pressure condition. We then open the fluid lines to let the butane gas escape. Brine is injected into the sample the same way as for butane. Samples are coated with an impermeable polyimide film (Kapton), over which semiconductor strain gages are glued to measure rock deformations at seismic frequencies. This film keeps moisture inside the rock, prevents nitrogen diffusion and eliminates the Biot-Gardner effect observed in unjacketed rocks [*Gardner*, 1962; *White*, 1986; *Mörig and Burkhardt*, 1989].

[17] All dry samples, except sample B, are initially humidified by storing the samples in a humidifying chamber at 98% humidity for 2 weeks, to create matrix softening that results from moisture in the pore space. *Clark et al.* [1980] showed that introducing water vapor (~1% water saturation in pores) to oven dry samples can significantly reduce the rock bulk and shear moduli, and increase attenuation. The water content is not expected to be less than 1% in reservoirs, as even gas filled reservoirs have irreducible water in the pore space. The rock sensitivity to water vapor is directly related to the pores surface area. Nonetheless, we will show here that as the brine saturation of the rock increases, the rock frame softens. Such weakening could well be observed in reservoirs where brine displaces the original gas or fluid.

[18] Figure 4 is a drawing of the sample setup and a sketch of the recorded low-frequency strains for the different gages. At seismic frequencies, moduli and attenuation are measured by applying a sinusoidal stress to the rock and measuring the resulting strain in different directions on the rock sample and on the reference material (aluminum). The measured strain amplitudes are low ($\sim 10^{-7}$), the same

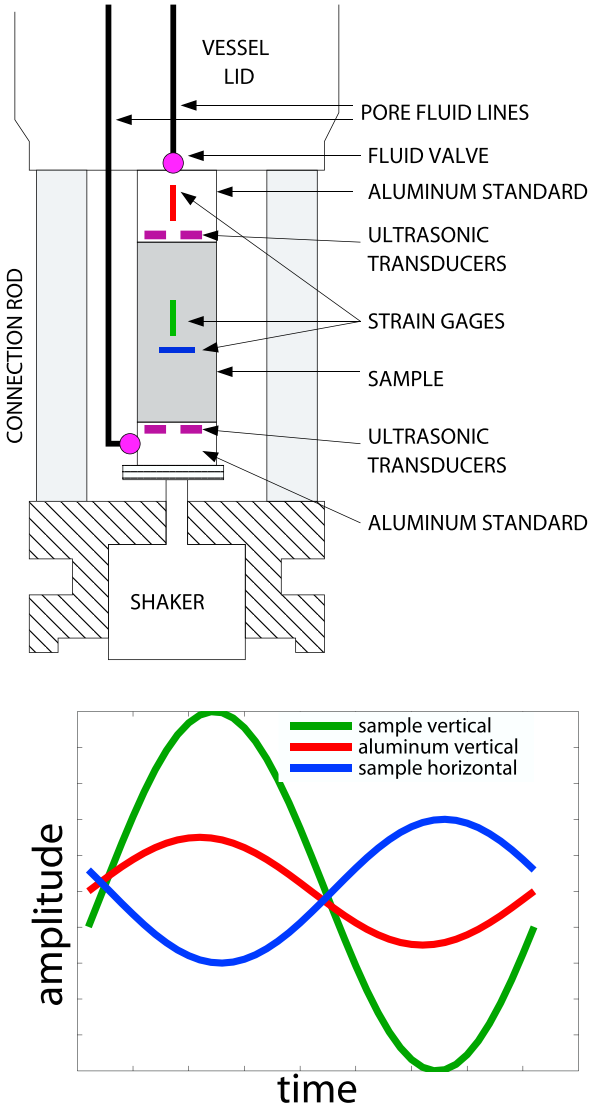

Figure 4. Sample schematic for measurements at seismic frequencies (with strain gages) and ultrasonic frequencies (with transducers). Confining pressure is applied to the whole system, and pore pressure is controlled through the pore fluid lines. The strain gage responses for the three gage locations are also sketched.

amplitude as the deformation imposed on the reservoirs in the field by seismic waves. The samples and reference are cylindrical and are attached in series with the cylinder axis coinciding with the axis of applied stress. The moduli are estimated from the amplitude of the strain signatures (for details, see *Batzle et al.* [2006]). To measure ultrasonic frequencies, we use transducers embedded in the aluminum reference (Figure 4). We record the waveform transmitted through the rock core [*Birch*, 1960]. From the measured time of flight and sample length, we estimate the P and S wave velocities and from these, the rock moduli. Samples with visible heterogeneity or large vugs the size of the strain gages (~0.5 cm) are avoided because the gages will measure the properties of the heterogeneity, biasing the estimate of attenuation. For the ultrasonic pulse, these heterogeneities can create scattering losses.

[19] The whole system as shown in Figure 4 is lowered into a high-pressure vessel. Confining (hydrostatic) pressure (P_c) is applied with nitrogen gas; while the pore pressure (P_p) is controlled through the pore fluid lines with different types of fluids. We present attenuation data recorded under differential pressure (P_d): $P_d = P_c - P_p$. Velocity and attenuation data are measured at P_d = 31 MPa differential pressure for samples 100 and 200, P_d = 24 MPa for sample 300, and for samples B and C, P_d = 21 MPa. For all rocks, P_p was held constant at 3.5 MPa. Because the sample setup is pressurized with nitrogen gas, for safety reasons the system is not able to quite reach the reservoir's confining pressure. However, the pressures in the experimental setup are close to the reservoirs differential pressure (see Table 1).

[20] In our experiments, we estimate Q_E^{-1} and Q_S^{-1} at seismic frequencies, and Q_P^{-1} and Q_S^{-1} at ultrasonic frequencies. In a viscoelastic material, the strain lags in phase with respect to the stress. This phase lag (θ) can be described in terms of the complex modulus: $Q^{-1} = \mathrm{Im}[M^*]/\mathrm{Re}[M^*] = \tan\theta \approx \theta$. Because the phase lag is small, we can approximate the tangent by the angle itself. In our low-frequency experiments, attenuation is estimated from the phase lags between the different strains. The phase is obtained by using a lock-in amplifier. We assume that the phase of the strain on the aluminum represents the phase of the applied stress. This is a reasonable assumption because the attenuation for aluminum is low ($Q^{-1} \sim 10^{-5}$). Thus, extensional attenuation (Q_E^{-1}) is estimated from the phase lag of the vertical strain on the rock and the reference aluminum. The vertical strain on the rock has the largest strain waveform amplitudes, yielding robustness in the estimate of Q_E^{-1}. To obtain the shear wave attenuation, we use the following relation [*White*, 1965]:

$$\frac{1}{Q_S} \simeq \frac{1}{Q_E} - \frac{\nu \tan(\theta_\nu)}{1+\nu} \tag{4}$$

where ν is Poisson's ration and θ_ν is the phase lag between the vertical and horizontal strain on the rock sample. Poisson's ratio at seismic frequencies is obtained from the ratio of the horizontal and vertical strain amplitude on the rock. The estimate of Q_S^{-1} is not overly sensitive to an error in ν. A ±10% bias in ν translates into a ±2% error Q_S^{-1}. *Winkler and Nur* [1982] derive equations that enable the estimation of a specific mode of attenuation for isotropic materials from two other attenuation modes and the Poisson's ratio. We estimate the P wave and the bulk compressibility attenuation from [*Winkler and Nur*, 1982]

$$\begin{aligned} \frac{(1-\nu)(1-2\nu)}{Q_P} &= \frac{1+\nu}{Q_E} - \frac{2\nu(2-\nu)}{Q_S} \\ \frac{1-2\nu}{Q_K} &= \frac{3}{Q_E} - \frac{2(\nu+1)}{Q_S} \end{aligned} \tag{5}$$

[21] For the ultrasonic data, attenuation is estimated by the spectral ratio method [*Toksoz et al.*, 1979; *Hauge*, 1981]. An aluminum sample of the same shape and dimensions as the rock sample is used as a reference material to establish the base spectra. Aluminum has a high bulk modulus (K = 76 GPa) and a high Q. The waveforms on the aluminum sample were measured at room conditions and under 31 MPa confining pressure, but there is no significant difference in the ultrasonic waveform or on the amplitude spectrum at these conditions. The direct arrivals for the sample and aluminum are windowed by a Hanning-type function, and the amplitude spectra are obtained from a discrete Fourier transform to these isolated events. Q is estimated from the logarithm of the ratio of amplitude spectra as a function of frequency. P and S wave attenuation are directly estimated from the waveforms, and we use the relations in equation (5) to estimate the remaining two attenuation modes.

4. Parameter Uncertainty

[22] Estimates of the error in our data are represented in terms of the standard deviation (σ) between our noisy observations and data predicted by an assumed true model (for details, see *Adam et al.* [2006]). For the low-frequency data, this is the standard deviation of our phase measurements and the Poisson's ratio. The repeatability or standard deviation of the phase measurements with our lock-in amplifier is on average 0.03 degrees [*Gautam*, 2003]. One standard deviation of the Poisson's ratio (ν) is on average 0.002. These phase and ν standard deviations are propagated to estimate the error in Q^{-1} at seismic frequencies. On average, at low frequencies, one standard deviation in $1/Q_K$, $1/Q_P$, $1/Q_E$, $1/Q_S$ are 0.0042, 0.0090, 0.0023, 0.0031, respectively. The average σ in P wave and S wave seismic velocity are 121 and 42 m/s, respectively.

[23] Attenuation at ultrasonic frequencies is estimated by the spectral ratio method on the recorded waveforms. On average, the estimated standard deviation for $1/Q_K$, $1/Q_P$, $1/Q_E$, $1/Q_S$ at ultrasonic frequencies are 0.0019, 0.0007, 0.0019, 0.0012, respectively. The average σ for P wave and S wave ultrasonic velocities are 22.4 m/s and 7.8 m/s, respectively.

[24] We cannot quantify the bias estimate on our Q estimate because we do not know the true model, but we can estimate part of a bias on Q on the basis of the difference in attenuation estimates between two methodologies. The frequency shift [*Quan and Harris*, 1997] and the spectral ratio methods assume Q to be frequency-independent, but Q is estimated differently by integrating or taking the ratio of amplitude spectra, respectively. On average, the

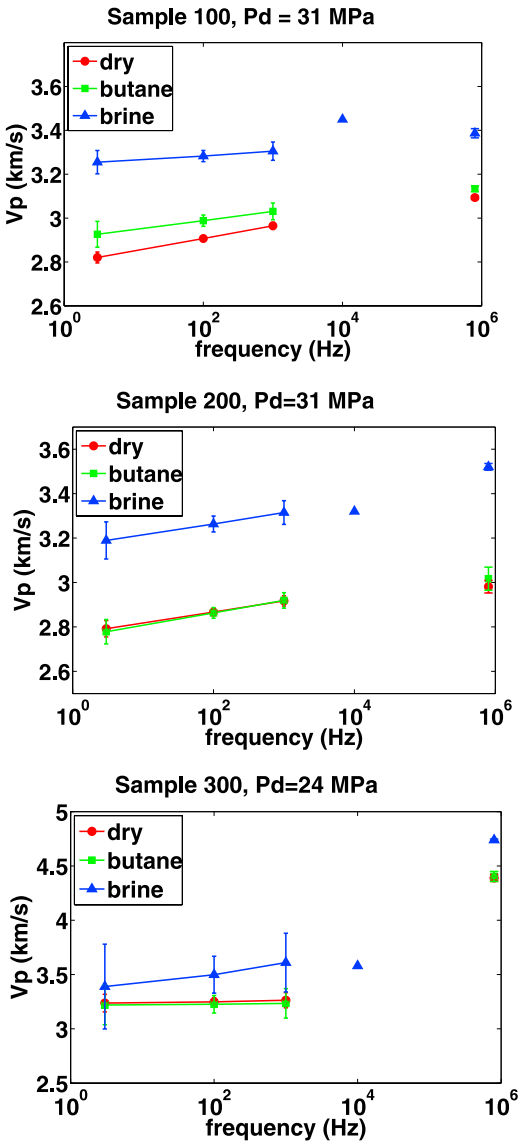

Figure 5. P wave velocity as a function of frequency for samples 100, 200, and 300, measured dry and fully saturated with liquid butane and brine. A linear fit is applied to the low-frequency data (3, 100, and 1000 Hz). The data at 10^4 Hz are obtained from the sonic logs. One σ for the ultrasonic data is the size of the markers. Pd, differential pressure.

ultrasonic attenuation estimates between these two methods differ by 18%. Other sources of bias on Q are possible if we have errors in the following two parameters. (1) If there is a ±10% variation in this window size, the error in Q is ±20% because we either include late arrivals or the window is not long enough to contain the whole amplitude information of the direct arrival. (2) If there is a ±5% error in the picked first arrival time, Q has an error of ±6%.

5. Dispersion

[25] Figure 5 shows the P wave velocity as a function of frequency for samples 100, 200, and 300, estimated at seismic frequencies between 10 and 1000 Hz, and accompanied by a single ultrasonic data point at 0.8 MHz. We plot the low-frequency velocity at three representative points (10, 100, and 1000 Hz) obtained from the parameter estimation and error analysis described in section 4. The data points near 10^4 Hz are obtained from sonic log data in the wells from which the rock samples were cored. This velocity is an average over a 0.6 m depth range centered at the sample depth. From the resistivity and bulk density logs, we conclude that the samples were extracted from brine-saturated reservoir intervals. Overall, the P wave velocity for the three samples consistently increases with frequency. At low frequencies, sample 300 has large error bars in the velocity, so the velocity in this sample could be interpreted as nondispersive in the seismic frequency range.

[26] There are two reasons why the ultrasonic velocity is higher than seismic and log velocities. High velocities at ultrasonic frequencies can result from the bulk stiffening due to pore fluid pressures being unable to reach equilibrium within one wave period [*Biot*, 1956b]. At low frequencies there is enough time for the pore fluid pressure to relax, the system is, therefore, more compliant, which results in lower velocities. Our observed velocity dispersion is in agreement with those from the broad frequency range experiment on sandstones by *Sams et al.* [1997] and *Best and Sams* [1997]. This velocity dispersion could be modeled by existing dispersive media theories [*Biot*, 1956a, 1956b; *O'Connell and Budiansky*, 1977; *Dvorkin et al.*, 1995; *Müller and Gurevich*, 2005]. However, choosing the wave dispersion mechanisms that best describe our data is beyond the scope of this paper.

[27] An alternative explanation why the ultrasonic velocity is higher than for seismic and log frequencies is that the ultrasonic wave propagation is path-dependent. This phenomenon is particularly relevant given our transducer size. Each ultrasonic crystal (P and S wave) in our transducer package has a diameter of 0.75 cm, compared to the aluminum casing diameter of 3.75 cm. Small transducers are used because the aluminum casing is also our reference material for the strain measurements, and a large crystal embedded into the casing would change the elastic properties of the aluminum. Because the transducer face is small with respect to the sample diameter, the generated high-frequency wave can propagate through the fastest path in the sample. For a heterogeneous sample with high and low compressibility regions, a portion of the ultrasonic pulse preferentially propagates along incompressible, high-speed wave regions according to Fermat's principle.

[28] For sample 300, the log data agree better with the low-frequency data than with the ultrasonic data (Figure 5). From the CT scan for sample 300 (Figure 2), zones of high and low compressibility are aligned with the pulse propagation direction, accentuating the fast path phenomenon. The ultrasonic energy then can traverse this heterogeneous sample more quickly, leading to an overestimate of the average wave speed of sample 300. This analysis is qualitative at this point, but it shows how a relatively high ultrasonic velocity can be due to fluid-rock dispersion as well as path dependence dispersion.

6. Attenuation Modes

[29] Figures 6 to 10 show the different attenuation modes for all the samples as a function of frequency for three pore-

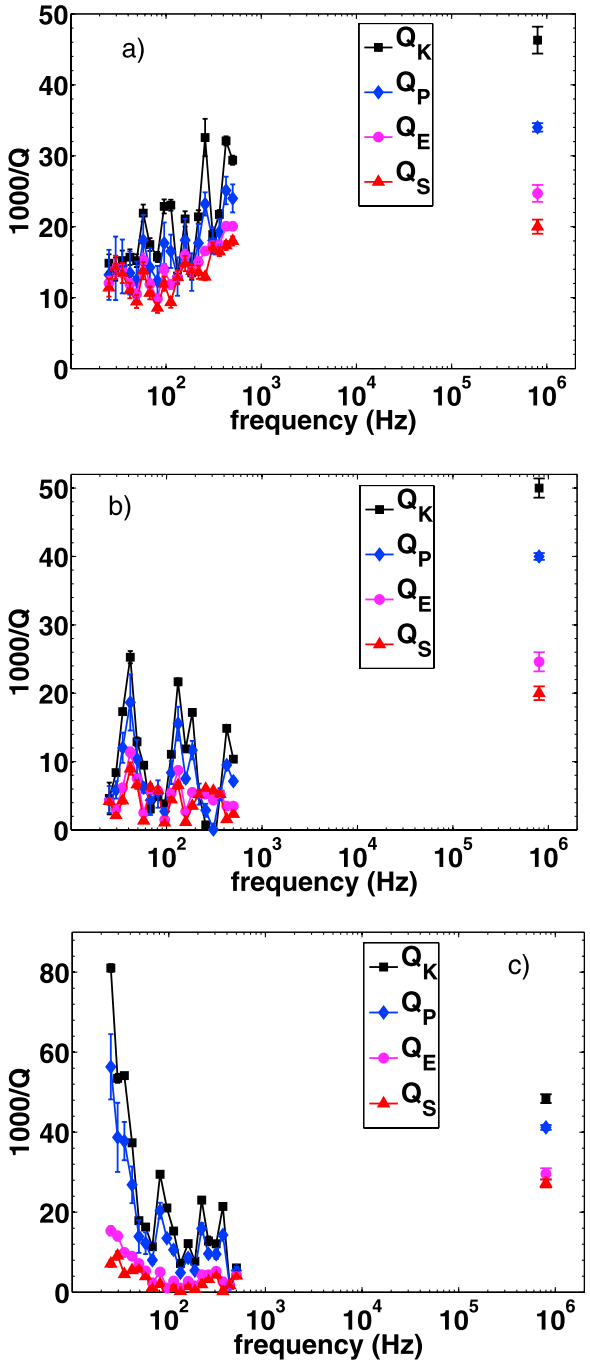

Figure 6. P wave, S wave, and extensional and bulk compressibility attenuation for sample 100 at 31 MPa differential pressure. The sample is measured (a) dry (humidified), (b) 100% saturated with liquid butane, and (c) 100% saturated with brine.

filling fluids. For low-frequency data we first estimate extensional and shear wave attenuation, and from these and the Poisson's ratio we obtain bulk and P wave attenuation. For ultrasonic data, we use the P and S wave attenuation estimates to calculate the extensional and bulk attenuation. For most samples and frequencies, bulk compressibility losses dominate the shear wave attenuation for dry (humidified) and 100% saturated samples. These carbonate samples show that relation (2), previously interpreted as a condition of partial saturation [*Winkler*, 1979], governs our fully saturated carbonate samples. For sample 300, the P wave transducer failed; therefore, there is no ultrasonic frequency P wave attenuation data. We also did not acquire the ultrasonic attenuation for samples B and C because we did not have the ultrasonic aluminum standard measurements to go with it. Sample 300 has low Q, and

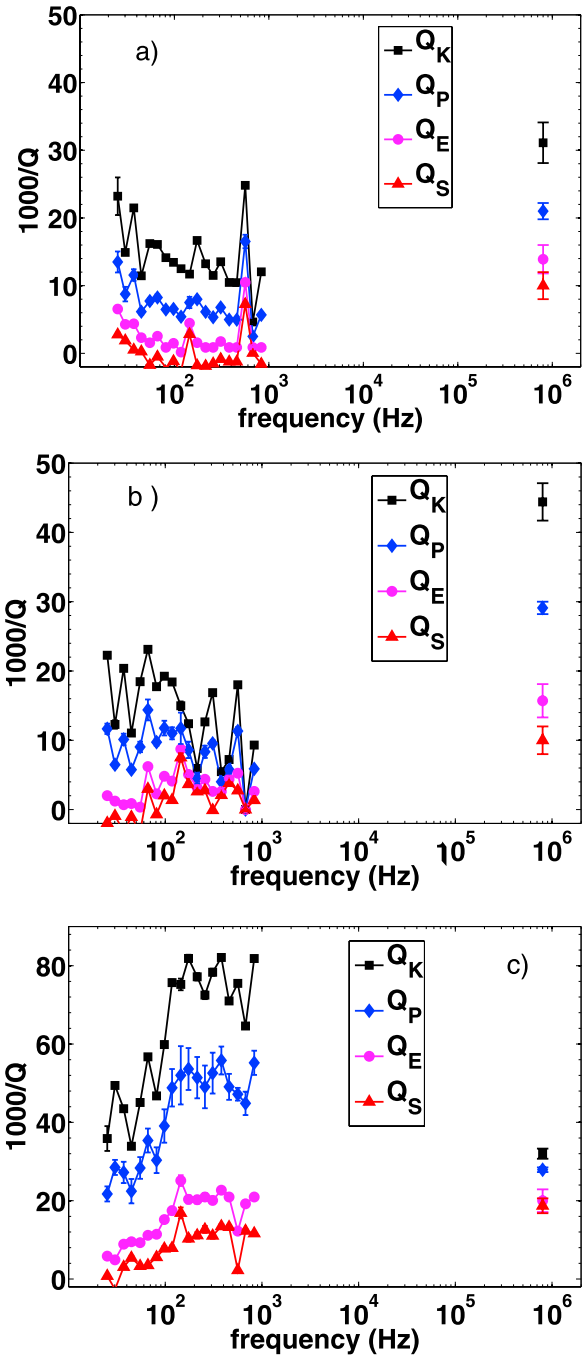

Figure 7. P wave, S wave, and extensional and bulk compressibility attenuation for sample 200 at 31 MPa differential pressure. The sample is measured (a) dry (humidified), (b) 100% saturated with liquid butane, and (c) 100% saturated with brine.

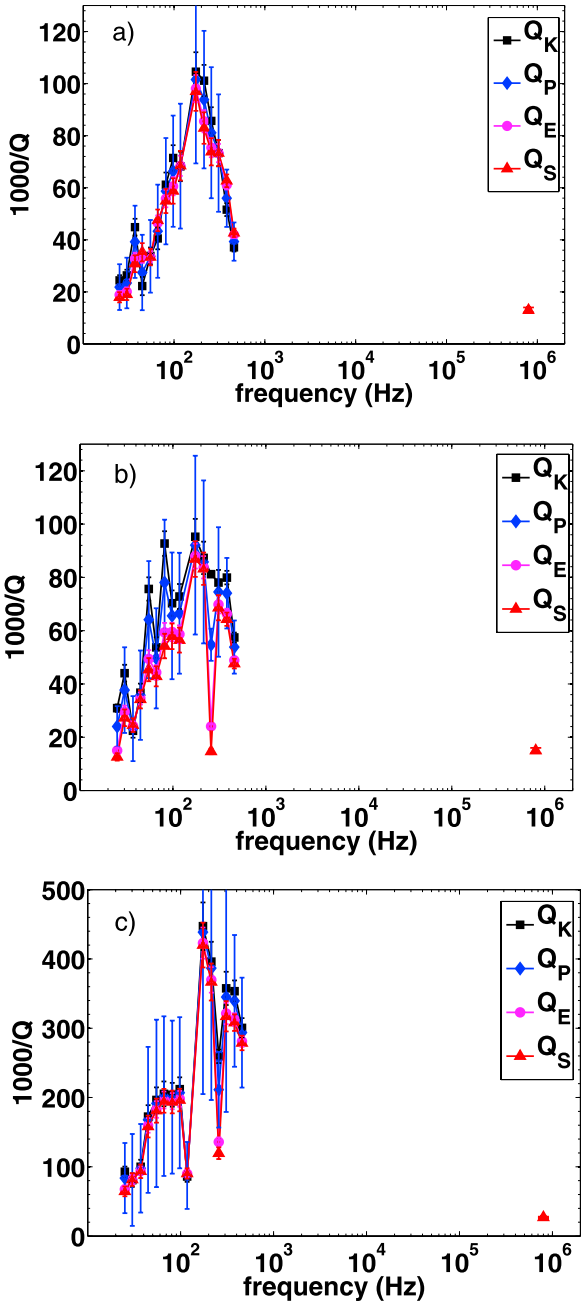

Figure 8. P wave, S wave, and extensional and bulk compressibility attenuation for sample 300 at 24 MPa differential pressure. The sample is measured (a) dry (humidified), (b) 100% saturated with liquid butane, and (c) 100% saturated with brine.

overall the attenuations are equal for all modes. High attenuation is probably responsible for the inability to distinguish between attenuation modes.

[30] There are two ways we try to ensure full saturation of the connected pore space. First, we calculate the connected pore volume from the porosity and dimensions of the sample. We then monitor the fluid flow into the sample until there is no more flow from the pump to the sample. The volume of injected fluid is within 2% of the computed pore volume. Second, we observe the bulk modulus as a function of brine saturation. Figure 11 shows the bulk modulus as a function of saturation for sample 300. The addition of pore fluid stiffens the sample, which we observe as an increase in bulk modulus. The significant increase of the bulk modulus at 100% saturation supports the assumption that sample 300 is fully saturated. Observe that a small amount of gas (~8%) drops the bulk modulus close to its dry sample value for seismic frequencies. For ultrasonic frequencies, the bulk modulus starts increasing at a saturation lower (~23%) than for the seismic frequencies

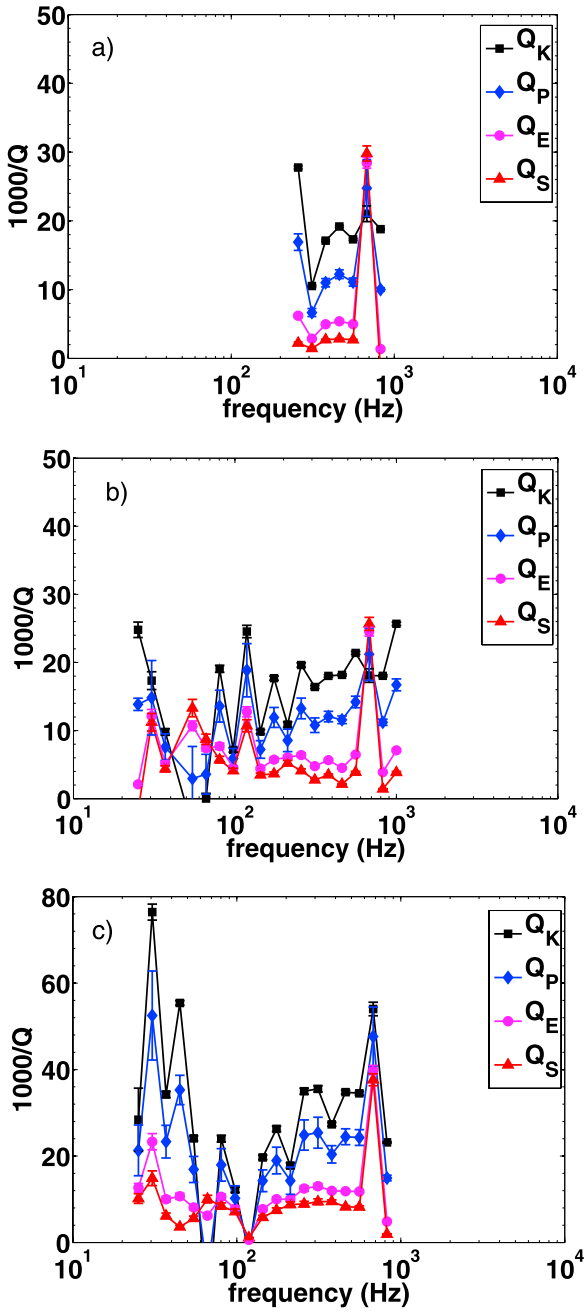

Figure 9. P wave, S wave, and extensional and bulk compressibility attenuation for sample B at 21 MPa differential pressure. The sample is measured (a) dry (humidified), (b) 100% saturated with liquid butane, and (c) 100% saturated with brine.

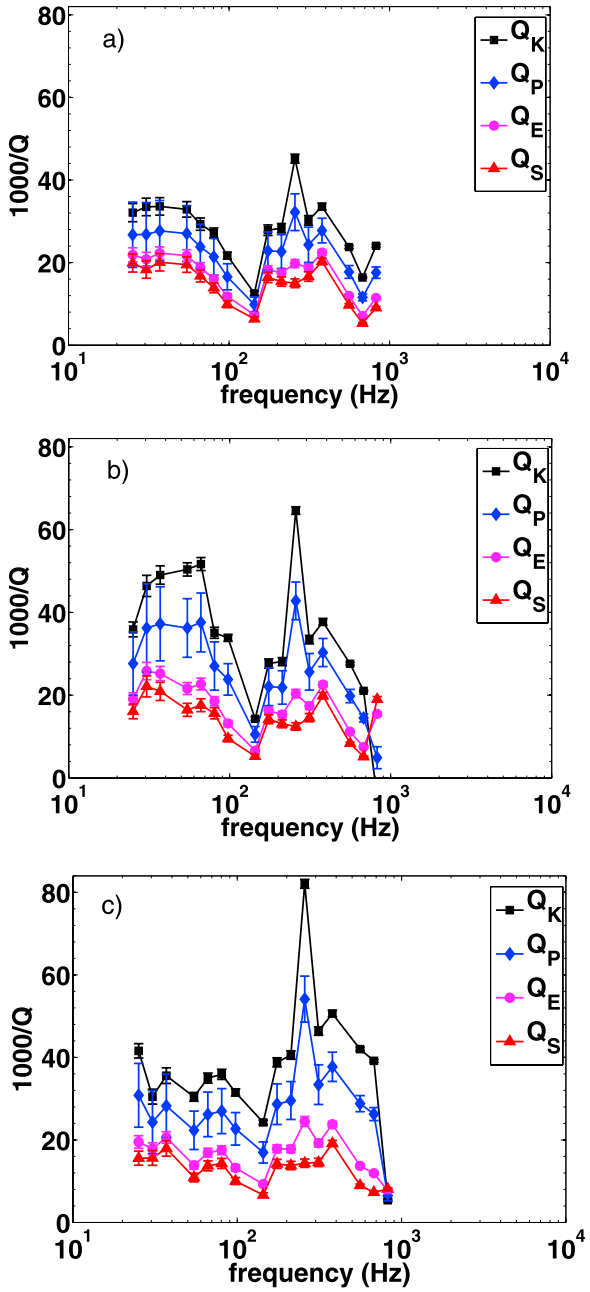

Figure 10. P wave, S wave, and extensional and bulk compressibility attenuation for sample C at 21 MPa differential pressure. The sample is measured (a) dry (humidified), (b) 100% saturated with liquid butane, and (c) 100% saturated with brine.

(~62%). As mentioned in section 5, the velocity or modulus increase with frequency can result from rock-fluid dispersion mechanisms or path effects. Samples partially saturated by imbibition can have regions that are saturated while others remain dry. These saturated regions can form preferential high-speed paths with high bulk moduli.

[31] The dominance of the bulk over shear attenuation for our saturated samples can be explained two ways. The first is related to the fact that relations (1) and (2) are associated with full or partial saturation respectively. This interpretation is based on a conceptual model of two identical low aspect ratio pores (cracks) perpendicular to each other at their tips [see *Winkler and Nur*, 1982, Figure 15]. Because we are dealing with carbonate rocks of complex texture, the variety of pore shapes may not be well described by this two crack model. Thus, the saturation state of carbonate rocks might not be possible to determine from the relation among the different attenuation modes. Second, *Dvorkin et al.* [1995] show that squirt flow from softer pores or cracks to stiffer pores in fully saturated rocks can predict that the compressional wave attenuation is greater than the shear wave losses. This model is hard to implement with our data, because attenuation for low pressure is calculated from data at high pressure, where cracks or compliant pores are assumed to be closed. Also, pore scale squirt models are probably not dominant at seismic frequencies [*Pride et al.*, 2004], but the same idea regarding losses has been extended to seismic frequencies by substituting the notion of pores by mesoscopic regions [*Pride et al.*, 2004; *Masson and Pride*, 2007].

[32] In our carbonate samples, no microcracks are observed from the thin sections, but the existence of compliant pores is interpreted from the pressure dependence of the shear modulus in Figure 12. At lower pressures, compliant pores open, softening the rock frame and lowering the modulus and velocity. All the samples show similar pressure dependence for the modulus and velocity as for Figure 12. Because of the textural complexity of carbonate rocks and because hydrostatic stress is applied, compliant pores can remain open even at high differential pressure, creating soft rock regions. Therefore, losses resulting from fluid movement from softer to stiffer regions is possible for our carbonate samples at high differential pressures, and can result in compressional losses dominating over shear losses.

[33] There are several experimental challenges when measuring attenuation that must be accounted for when interpreting the results plotted in Figures 6–10. First, the fluid lines in Figure 4 have a manual valve which we close when acquiring low-frequency data. The fluid lines are designed to allow high fluid flow into and out of the sample. Unless the valve is completely closed, the applied stress at low frequencies (<50 Hz) creates significant fluid movement from the sample and into the fluid lines. This fluid flow effect is illustrated in Figure 6c for frequencies

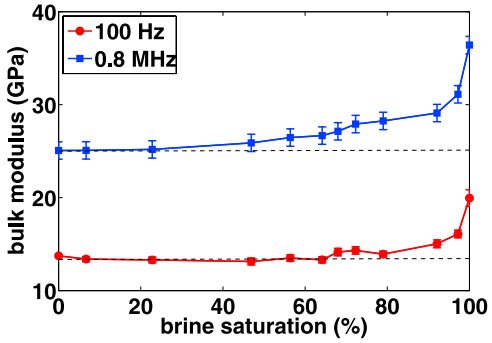

Figure 11. Bulk modulus as a function of brine saturation for sample 300 at seismic and ultrasonic frequencies. At 100 Hz, the bulk modulus increases 25% from 97% to 100% brine saturation.

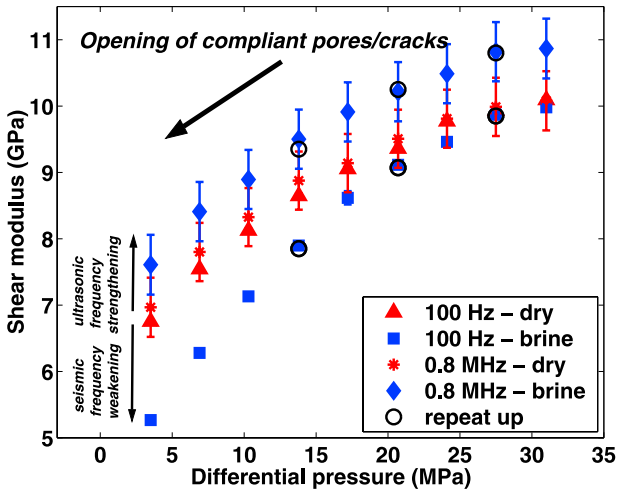

Figure 12. Sample C showing shear modulus weakening and strengthening at seismic and ultrasonic frequencies respectively. Measurements are performed from high to low differential pressures. Circles represent repeated differential pressures going from low to high differential pressures after the initial unloading cycle was finalized. Note that as we decrease the differential pressure, more compliant pores and cracks open. Error bars are one standard deviation (one σ for the seismic frequency data is contained in the size of the symbol).

less than 50 Hz, for which high attenuation is not related to the viscoelastic properties of the rock, but to a valve malfunction.

[34] A second challenge is that the low-frequency apparatus has system resonances at frequencies that depend on the vessel as well as the geometry and properties of the rock and aluminum samples. Resonance peaks at 150 and 257 Hz affect the attenuation measurements in Figure 8c. This resonance is evidenced by the attenuation peaks at those two frequencies, biasing the attenuation estimates in the 150 to 1000 Hz range. Therefore, to avoid the attenuation instability generated by the system resonances for sample 300, we only analyze frequencies between 10 and 100 Hz.

[35] A third challenge is to interpret how the heterogeneous rock texture observed on sample 300 can affect the low-frequency attenuation and modulus estimates. Twelve strain gages are glued on the sample and reference in groups of three every 90 degrees. One of the four sample sides is sketched in Figure 4. Gages on the 0° and 180°, and 90° and 270° faces are averaged into one strain during the acquisition recording. We then average the resulting 0°–180° and 90°–270° strains into one final strain estimate. Therefore, significant heterogeneity on one or more of the sample faces can affect the estimate of modulus and attenuation through this averaging process. It is possible that for sample 300, the textural heterogeneity evidenced in Figure 2 causes the high attenuation values plotted in Figure 8. Another possibility, however, is that because this sample has the largest permeability of the five measured samples, the high fluid mobility is responsible for the increased attenuation. The attenuation for sample 300 between 10 and 100 Hz is frequency-dependent, increasing with increasing frequency.

[36] In general, directly correlating attenuation between seismic and ultrasonic frequencies is not straightforward. At exploration seismic frequencies (10 to 100 Hz), all samples but sample 300 show that attenuation is frequency-independent (Figures 6 to 10). However, for frequencies between 10 and 1000 Hz, attenuation estimates increase with increasing frequency for samples 100, 200, and 300. For a single relaxation mechanism, attenuation as a function of frequency is described by a bell-shaped curve with a peak which can depend on the rock permeability and fluid viscosity [*Biot*, 1956a, 1956b; *Mavko and Nur*, 1979]. Multiple attenuation mechanisms can result in multiple maxima. Our data (with a gap in observations between 10^3 and 10^6 Hz) does not require a more complex model than the most conservative model of a single relaxation mechanism. For the measured samples, the attenuation maximum may be located in the data gap between 10^3 and 10^6 in Figures 7c and 8, or at a frequency greater than 10^6 Hz in Figures 6, 7b, and 7c.

7. Bulk Modulus Attenuation and Fluids

[37] Figure 13 shows the estimated bulk modulus attenuation as a function of frequency for all measured fluids and samples. Attenuation is nonzero when samples are dry (humidified) because a fluid layer on carbonate grains can increase attenuation compared to an oven-dry sample when the stress generated by the passing wave creates movement of the small amount of water [*Clark et al.*, 1980; *Murphy et al.*, 1986; *Winkler and Nur*, 1982]. *Winkler et al.* [1979] analyze the effect of frictional loss with strain for sandstone samples, and show that strain becomes a loss mechanism for strain amplitudes greater than 10^{-6}. In their study, for dry or slightly saturated samples measured at strains between 10^{-7} and 10^{-6}, extensional attenuation is nonzero ($Q_E \approx 100$), but the loss mechanism is not attributed to friction. We do not attribute our observed attenuation to friction between grains because our measurements are at a single strain amplitude of 10^{-7}.

[38] Attenuation estimates when the rock is dry or fully saturated with butane are comparable for all samples, but we observe an increase in attenuation when brine replaces liquid butane. The changes from butane to brine resemble a reservoir fluid substitution process. We observe that the P wave attenuation increases by 150% to 400%, depending on the sample, when a brine replaces a light hydrocarbon in the pore space. By comparison, the P wave velocity changes only 4% to 10% when brine substitutes liquid butane in these samples. For a producing field and if time-lapse data are available, this attenuation sensitivity to fluids may be useful as an additional seismic attribute for dynamic reservoir monitoring.

[39] Samples 100 and 200 have significantly different attenuation when saturated with brine, although petrographically they are similar. Sample 200 may have larger pore throats than sample 100, so that the induced pore pressure gradients responsible for attenuation will reach equilibrium differently for these two samples. It is important to keep in mind that our samples remain undisturbed in the apparatus during the exchange of fluids. There is no handling of the sample between attenuation measurements at varying saturating conditions. Therefore, even if the absolute values of

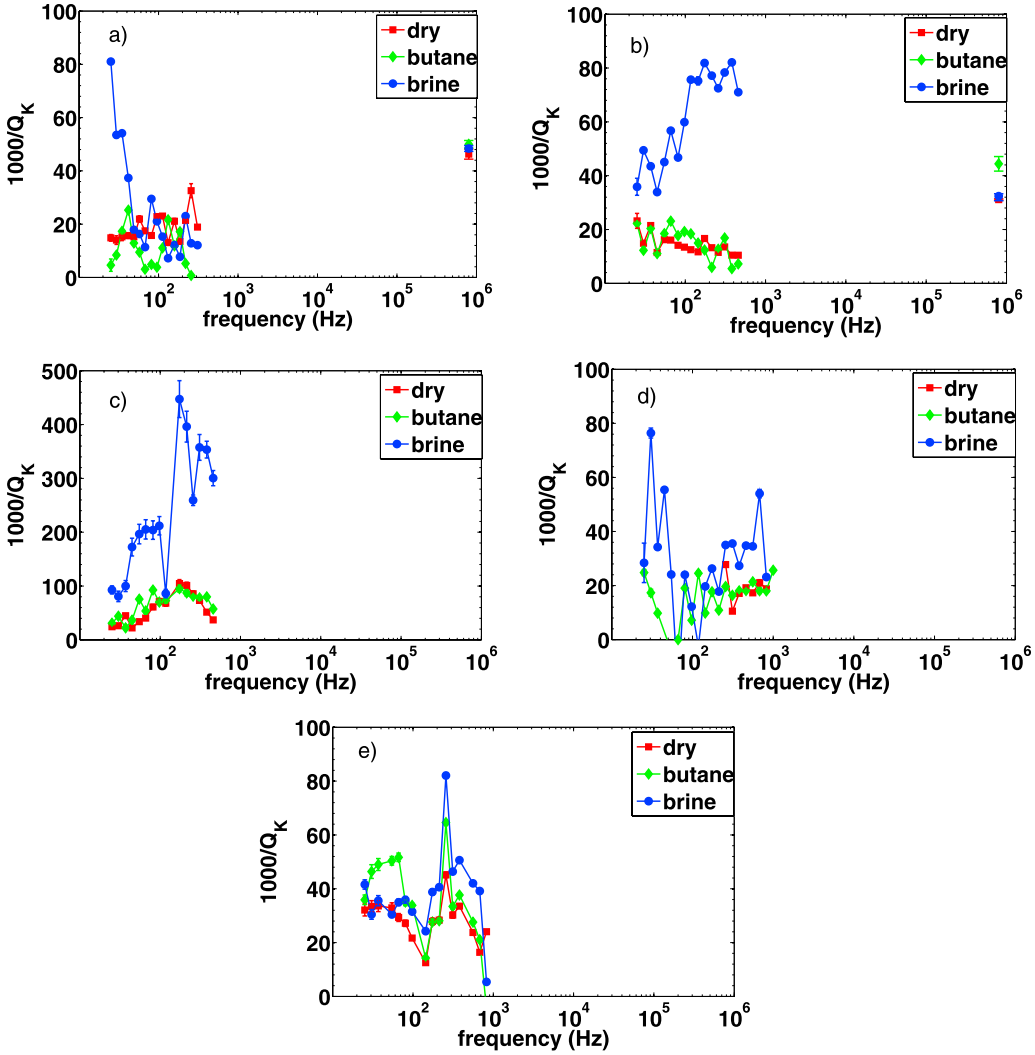

Figure 13. Bulk compressibility attenuation for all samples: (a) 100, (b) 200, (c) 300, (d) B, and (e) C. Dry measurements were performed with the samples humidified, not oven dry. Therefore, some water exists in the pore space. Butane and brine test are run at full saturation. The differential pressures are as reported in Figures 6 to 10.

the attenuation might have some bias, especially for sample 300, we expect this bias to be consistent between fluids.

[40] We now describe possible reasons for the attenuation to increase when brine substitutes liquid butane. Fluid viscosity controls the frequency at which the maximum peak of attenuation occurs. At 3.5 MPa and 25°C, the viscosity of liquid butane and brine are similar, 0.2 cP and 1 cP, respectively. Nonetheless, the small viscosity difference between water and butane could still affect the attenuation of the rock [*Gautam*, 2003; *Best et al.*, 1994]. Another possible reason for high attenuation in brine-saturated carbonates is related to the weakening of the rock frame upon water saturation.

[41] Figure 12 shows the shear modulus as a function of differential pressure for sample C at 100 Hz and ultrasonic frequencies (0.8 MHz). We observe that as differential pressure decreases and compliant pores open, the rock shear modulus decreases (weakens) from dry (humidified) to fully brine saturated. Therefore, there is a correlation between increasing numbers of compliant pores and an increase in the shear modulus weakening. If the solid frame of the rock does not change, the rock shear modulus is not sensitive to the saturating fluid, because the shear modulus of fluids is zero. However, the modulus decrease due to brine can be explained by the weakening of the rock frame resulting from the interaction of a polar fluid such as water with the solid frame of the rock [*Khazanehdari and Sothcott*, 2003; *Adam et al.*, 2006; *Risnes et al.*, 2005]. Rock surface energies or solid bounds between grains can break in the presence of water, weakening the rock. This process increases the pore space and can increase attenuation. *Spencer* [1981] measured extensional modulus attenuation in a fully water saturated limestone at low frequencies (10–100 Hz), and showed that attenuation is caused by the reduction in surface energy in the grains (matrix softening). *Vo-Thanh* [1995] shows that the shear wave attenuation depends on the amount of water saturation in limestone and sandstone. We observe that frame weakening is also dependent on the amount of water in the pore space. This rock frame softening is shown in Figure 14, where the shear modulus weakens by increasing brine saturation for sample 300.

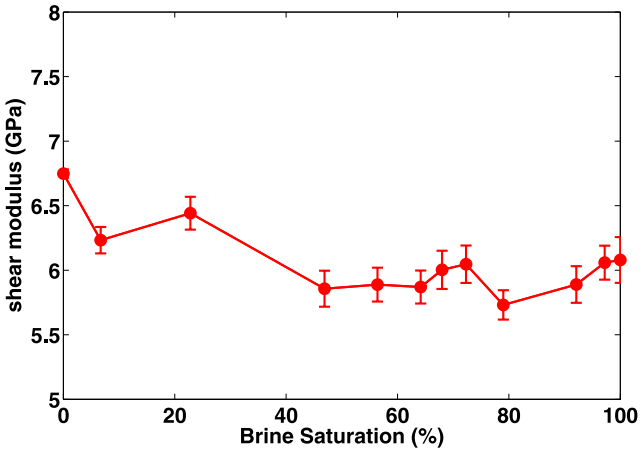

Figure 14. Shear modulus weakening with brine saturation for sample 300 at 100 Hz and 21 MPa differential pressure.

[42] An alternative attenuation mechanism can result from local fluid flow between the gap in the grain contact and the adjacent pores [*Murphy et al.*, 1986]. This wave attenuation is dependent on the saturation state of the rock, and the frequency at which the peak of maximum attenuation occurs. The latter is largely a function of the fluid and the size of the grain contact gap. As the aspect ratio of this gap decreases, the attenuation maximum moves toward lower frequencies. After brine saturation, grain contacts could have lower aspect ratios (solid bounds break), which under the grain contact loss mechanism means that the maximum attenuation peak shifts to lower frequencies. For our limited low-frequency interval, a peak is hard to define. Nonetheless, the attenuation maximum shift to lower frequencies can be observed as an increase in attenuation (see, e.g., Figure 13b). Finally, for our samples, brine is not believed to be dissolving the carbonate grains, because Figure 12 shows that the frame weakening process is reversible (black circles). In conclusion, the increase of soft regions in the rock due to brine (newly opened grain contacts compared to dry or butane-saturated carbonates), can increase the differential fluid-rock movements, and therefore attenuation.

8. Numerical Modeling

[43] In sections 6 and 7 we have suggested reasons why $Q_K^{-1} > Q_S^{-1}$ in our carbonate samples. Here we support these interpretations of measured attenuation with numerical modeling constrained by our estimated values of elastic moduli and velocities. The amplitude and phase of our measured waveforms provide estimates of the elastic moduli and attenuation, respectively. These two attributes can be assumed independent. For an elastic sample, the strain amplitude yields moduli and the strain phase shifts are zero. That same sample under different saturation conditions can behave viscoelastically, with the same strain amplitude as for the elastic sample, but with a nonzero phase shift. On the basis that phase strain amplitude is independent of phase, we model attenuation from the measured modulus and show that $Q_K^{-1} > Q_S^{-1}$.

[44] The modulus frequency dependence in a material is directly related to the attenuation. In the extreme case of no modulus dispersion, there is no attenuation; which is a fundamental relation described by the Kramers-Kronig equations. In practice, *Cole and Cole* [1941] obtain an equation that describes the complex modulus (M^*) dispersion as a function of frequency (w):

$$M^*(w) = \frac{(M_0 - M_\infty)}{1 + (iw\tau_0)^{1-\alpha}} + M_\infty \tag{6}$$

where M_0 and M_∞ are the moduli at zero and infinite frequency, respectively; τ_0 is the relaxation time and α is a parameter that controls the curvature of the S-shaped modulus dispersion; α is bounded between 0 and 1, and if $\alpha = 0$, equation (6) reduces to the modulus dispersion relation for a standard linear solid or Debye model. The α value controls the amplitude of the attenuation peak.

[45] We use equation (6) to model attenuation under the assumption that there is only one relaxation mechanism (i.e., one attenuation peak) between 10 and 10^6 Hz. We model the imaginary part of the complex modulus by applying a least squares fit to the real part of the measured modulus. We use the 3 Hz data as M_0, the ultrasonic data point as M_∞, and τ_0 and α follow from the best fit to the modulus versus frequency data. We model attenuation by taking the ratio of the imaginary and real parts of the modeled complex modulus. The solid lines in Figures 15a and 15b show the best fit to the real part bulk modulus and the modeled attenuation for sample 100 saturated with brine, respectively.

[46] Our measurements cover a large range of frequencies, but within 3 orders of magnitude (10^3–10^6) we only have one datum. Modeling attenuation as a function of frequency is highly sensitive to this ultrasonic datum. To show this sensitivity, we vary the ultrasonic data point. Twenty ultrasonic bulk moduli are generated from a Gaussian distribution of the ultrasonic errors. The dashed lines in Figure 15a are the best fits for each of the 20 ultrasonic points. The corresponding modeled attenuation are plotted as dashed lines in Figure 15b. For the large range of possible ultrasonic bulk modulus, the modeled attenuation peak ($1000/Q$) can vary from 25 to 75. Therefore, quanti-

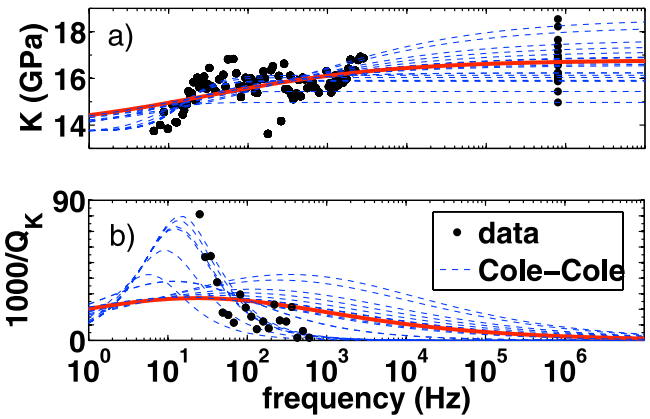

Figure 15. (a) Bulk modulus and (b) attenuation for sample 100 fully brine saturated. Dots are the measured data, and the lines are the modeled moduli and attenuation using the Cole-Cole relation.

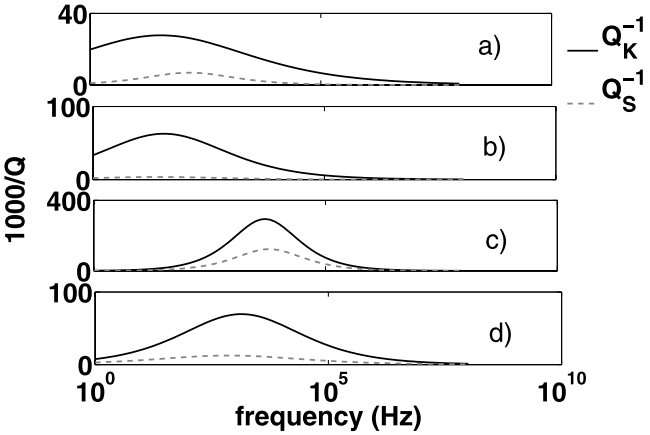

Figure 16. Modeled bulk and shear wave attenuation for fully brine saturated samples: (a) 100, (b) 200, (c) 300, and (d) C.

tatively estimating Q from measured bulk modulus is sensitive to the uncertainty in the ultrasonic data.

[47] Figure 16 shows that the modeled bulk attenuation is greater than the shear wave attenuation for the modeled brine-saturated samples. The same observation holds for when the samples are dry or fully saturated with liquid butane. The fact that bulk losses dominate over shear losses is in agreement with the experimental attenuation data shown in Figures 6 to 10. Sample B is not modeled because the ultrasonic bulk modulus is slightly lower than the low-frequency data; probably because the ultrasonic pulse is slowed down due to scattering in the horizontal layers in this sample.

9. Conclusions

[48] In contrast to clastics, our measurements in five carbonate rocks show that bulk modulus attenuation and compressional wave attenuation are greater than the shear wave attenuation when samples are fully saturated with either liquid butane or brine at reservoir conditions. This observation is consistent over a large range in frequencies (10–1000 Hz and 0.8 MHz) and is repeatable using two different experimental methodologies. Attenuation is observed to be frequency-independent for the exploration seismic frequencies (10–100 Hz) for four of five samples. From published laboratory data, the saturation state of sandstones could be interpreted based on whether the bulk or shear losses dominate; however, from our observations, this correlation will probably not be straightforward for carbonates. The sensitivity of attenuation, particularly the bulk modulus losses, to the type of fluid in the pore space is much greater than for velocities. Bulk modulus attenuation could change from 150% to 400% (depending on the sample) when brine replaces a light hydrocarbon. By comparison, the average compressional wave velocity changes by 7% for our samples.

[49] The laboratory measurements described here could aid in the interpretation of surface seismic data. In carbonates, the compressional wave seismic signature can be more sensitive to the wave losses than the shear wave data, especially when brine substitutes a light hydrocarbon. Even thought estimating intrinsic attenuation from surface seismic still faces some challenges, the recent improvements in data quality should make this estimation more reliable.

[50] **Acknowledgments.** We thank ADNOC, ADCO, and StatoilHydro for permission to publish the paper. We are grateful for the help and suggestions received from Manika Prasad, John Scales, and Ronny Hofmann. Finally, we thank ExxonMobil URC and Michelle Stoklosa for the petrographic analysis. We greatly thank the Associate Editor William Waite, and the reviewers Angus Best and William Murphy for their thorough reviews and suggestions that significantly improved this paper.

References

Adam, L., M. Batzle, and I. Brevik (2006), Gassmann's fluid substitution and shear modulus variability in carbonates at laboratory seismic and ultrasonic frequencies, *Geophysics*, *71*(6), F173–F183, doi:10.1190/1.2358494.

Agersborg, R., T. A. Johansen, M. Jakobsen, J. Sothcott, and A. Best (2008), Effects of fluids and dual-pore systems on pressure-dependent velocities and attenuations in carbonates, *Geophysics*, *73*(5), N35–N47, doi:10.1190/1.2969774.

Assefa, S., C. McCann, and J. Sothcott (1999), Attenuation of P- and S-waves in limestones, *Geophys. Prospect.*, *47*(3), 359–392, doi:10.1046/j.1365-2478.1999.00136.x.

Batzle, M., R. Hofmann, M. Prasad, G. Kumar, L. Duranti, and D.-H. Han (2005), Seismic attenuation: Observations and mechanisms, *SEG Tech. Abstr.*, *24*(1), 1565–1568, doi:10.1190/1.2147991.

Batzle, M. L., D. Hua Han, and R. Hofmann (2006), Fluid mobility and frequency-dependent seismic velocity—Direct measurements, *Geophysics*, *71*(1), N1–N9.

Best, A. I., and M. S. Sams (1997), Compressional wave velocity and attenuation at ultrasonic and sonic frequencies in near-surface sedimentary rocks, *Geophys. Prospect.*, *45*(2), 327–344.

Best, A. I., C. McCann, and J. Sothcott (1994), The relationships between the velocities, attenuations and petrophysical properties of reservoir sedimentary rocks, *Geophys. Prospect.*, *42*, 151–178.

Best, A. I., J. Sothcott, and C. McCann (2007), A laboratory study of seismic velocity and attenuation in near-surface sedimentary rocks, *Geophys. Prospect.*, *55*, 609–625.

Biot, M. A. (1956a), Theory of propagation of elastic waves in a fluid-saturated porous solid. I. Low-frequency range, *J. Acoust. Soc. Am.*, *28*(2), 168–178, doi:10.1121/1.1908239.

Biot, M. A. (1956b), Theory of propagation of elastic waves in a fluid-saturated porous solid. II. Higher frequency range, *J. Acoust. Soc. Am.*, *28*(2), 179–191, doi:10.1121/1.1908241.

Birch, F. (1960), The velocity of compressional waves in rocks to 10 kilobars: 1, *J. Geophys. Res.*, *65*, 1083–1102.

Cadoret, T., G. Mavko, and B. Zinszner (1998), Fluid distribution effect on sonic attenuation in partially saturated limestones, *Geophysics*, *63*(1), 154–160, doi:10.1190/1.1444308.

Clark, V. A., B. R. Tittmann, and T. W. Spencer (1980), Effect of volatiles on attenuation (Q^{-1}) and velocity in sedimentary rocks, *J. Geophys. Res.*, *85*, 5190–5198.

Cole, K. S., and R. H. Cole (1941), Dispersion and absorption in dielectrics. I. Alternating current characteristics, *J. Chem. Phys.*, *9*, 341–351.

Dvorkin, J., G. Mavko, and A. Nur (1995), Squirt flow in fully saturated rocks, *Geophysics*, *60*(1), 97–107, doi:10.1190/1.1443767.

Gardner, G. H. F. (1962), Extensional waves in fluid-saturated porous cylinders, *J. Acoust. Soc. Am.*, *34*(1), 36–39, doi:10.1121/1.1909010.

Gautam, K. (2003), Fluids effects on attenuation and dispersion of elastic waves, Master's thesis, Colo. Sch. of Mines, Golden.

Hauge, P. S. (1981), Measurements of attenuation from vertical seismic profiles, *Geophysics*, *46*(11), 1548–1558, doi:10.1190/1.1441161.

Khazanehdari, J., and J. Sothcott (2003), Variation in dynamic elastic shear modulus of sandstone upon fluid saturation and substitution, *Geophysics*, *68*(2), 472–481.

Lienert, B. R., and M. H. Manghnani (1990), The relationship between $Q_E^{(-1)}$ and dispersion in extensional modulus, E, *Geophys. Res. Lett.*, *17*(6), 677–680.

Lindquist, W. B., A. Venkatarangan, J. Dunsmuir, and T. Wong (2000), Pore and throat size distributions measured from synchrotron X-ray tomographic images of Fontainebleau sandstones, *J. Geophys. Res.*, *105*(B9), 21,509–21,528.

Lucet, N. (1989), Vitesse et atténuation des ondes élastiques et ultrasoniques dans les roches sous pression de confinement, Ph.D. thesis, Univ. de Paris VI, Paris.

Lucet, N., P. N. J. Rasolofosaon, and B. Zinszner (1991), Sonic properties of rocks under confining pressure using the resonant bar technique, *J. Acoust. Soc. Am.*, *89*(3), 980–990, doi:10.1121/1.400643.

Masson, Y. J., and S. R. Pride (2007), Poroelastic finite difference modeling of seismic attenuation and dispersion due to mesoscopic-scale heterogeneity, *J. Geophys. Res.*, *112*, B03204, doi:10.1029/2006JB004592.

Mavko, G. M., and A. Nur (1979), Wave attenuation in partially saturated rocks, *Geophysics*, *44*(2), 161–178.

Moore, C. H. (2001), Carbonate Reservoirs: Porosity Evolution and Diagenesis in a Sequence Stratigraphic Framework, *Dev. Sedimentol.*, vol. 55, Elsevier, Amsterdam.

Mörig, R., and H. Burkhardt (1989), Experimental evidence for the Biot-Gardner theory, *Geophysics*, *54*(4), 524–527, doi:10.1190/1.1442679.

Müller, T. M., and B. Gurevich (2005), Wave-induced fluid flow in random porous media: Attenuation and dispersion of elastic waves, *J. Acoust. Soc. Am.*, *117*(5), 2732–2741, doi:10.1121/1.1894792.

Murphy, W. F. (1982), Effects of partial water saturation on attenuation in Massilon sandstone and Vycor porous glass, *J. Acoust. Soc. Am.*, *71*(6), 1458–1468.

Murphy, W. F., K. W. Winkler, and R. L. Kleinberg (1986), Acoustics relaxation in sedimentary rocks: Dependence on grain contacts and fluid saturation, *Geophysics*, *51*(3), 757–766.

O'Connell, R. J., and B. Budiansky (1977), Viscoelastic properties of fluid-saturated cracked solids, *J. Geophys. Res.*, *82*, 5719–5736.

Paffenholz, J., and H. Burkhardt (1989), Absorption and modulus measurements in the seismic frequency and strain range on partially saturated sedimentary rocks, *J. Geophys. Res.*, *94*, 9493–9507.

Prasad, M., and R. Meissner (1992), Attenuation mechanisms in sands: Laboratory versus theoretical (Biot) data, *Geophysics*, *57*(5), 710–719, doi:10.1190/1.1443284.

Pride, S. R., J. G. Berryman, and J. M. Harris (2004), Seismic attenuation due to wave-induced flow, *J. Geophys. Res.*, *109*, B01201, doi:10.1029/2003JB002639.

Quan, Y., and J. M. Harris (1997), Seismic attenuation tomography using the frequency shift method, *Geophysics*, *62*(3), 895–905, doi:10.1190/1.1444197.

Risnes, R., M. Madland, M. Hole, and N. Kwabiah (2005), Water weakening of chalk—Mechanical effects of water–glycol mixtures, *J. Petroleum Science and Engineering*, *48*(1–2), 21–36, doi:10.1016/j.petrol.2005.04.004.

Sams, M. S., J. P. Neep, M. H. Worthington, and M. S. King (1997), The measurement of velocity dispersion and frequency-dependent intrinsic attenuation in sedimentary rocks, *Geophysics*, *62*(5), 1456–1464.

Scholle, P. A., and D. S. Ulmer-Scholle (2003), *A Color Guide to the Petrography of Carbonate Rocks: Grains, Textures, Porosity, Diagenesis*, AAPG Mem., 77.

Soroka, W. L., P. Melville, E. Kleiss, M. Al-Jenaibi, A. B. Al-Jeelani, H. H. Hafez, and A. Modavi (2005), Successful pilot onshore Abu Dhabi shows that 4D can monitor fluid changes in a giant middle east carbonate field, *SEG Tech. Abstr.*, *24*(1), 2430, doi:10.1190/1.2148212.

Spencer, J. W. (1979), Bulk and shear attenuation in Berea sandstone: The effects of pore fluids, *J. Geophys. Res.*, *84*, 7521–7523.

Spencer, J. W. (1981), Stress relaxation at low frequencies in fluid saturated rocks: Attenuation and modulus dispersion, *J. Geophys. Res.*, *86*, 1803–1812.

Toksoz, M. N., D. H. Johnston, and A. Timur (1979), Attenuation of seismic waves in dry and saturated rocks: I. Laboratory measurements, *Geophysics*, *44*(4), 681–690.

Vo-Thanh, D. (1995), Influence of fluid chemistry on shear-wave attenuation and velocity in sedimentary rocks, *Geophys. J. Int.*, *121*, 737–749.

White, J. E. (1965), *Seismic Waves; Radiation, Transmission, and Attenuation*, McGraw-Hill, New York.

White, J. E. (1986), Biot-Gardner theory of extensional waves in porous rods, *Geophysics*, *51*(3), 742–745, doi:10.1190/1.1442126.

Winkler, K. W. (1979), The effects of pore fluids and frictional sliding on seismic attenuation, Ph.D. thesis, Stanford Univ., Stanford, Calif.

Winkler, K., and A. Nur (1979), Pore fluids and seismic attenuation in rocks, *Geophys. Res. Lett.*, *6*, 1–4, doi:10.1029/GL006i001p00001.

Winkler, K. W., and A. Nur (1982), Seismic attenuation: Effects of pore fluids and frictional-sliding, *Geophysics*, *47*(1), 1–15, doi:10.1190/1.1441276.

Winkler, K. W., A. Nur, and M. Gladwin (1979), Friction and seismic attenuation in rocks, *Nature*, *277*, 528–531.

Wyllie, M. R. J., G. H. F. Gardner, and A. R. Gregory (1962), Studies of elastic wave attenuation in porous media, *Geophysics*, *27*(5), 569–589, doi:10.1190/1.1439063.

L. Adam and K. van Wijk, Department of Geosciences, Boise State University, 1910 University Drive, Boise, ID 83725, USA. (milaadam@boisestate.edu)

M. Batzle, Department of Geophysics, Colorado School of Mines, 1500 Illinois Street, Golden, CO 80401, USA.

K. T. Lewallen, ExxonMobil Upstream Research Company, 3120 Buffalo Speedway, Houston, TX 77098, USA.